Generation and processing of pseudo shear-wave data: Theory and case study

Vladimir Grechka* & Pawan Dewangan†

* *Shell International Exploration and Production, 3737 Bellaire Blvd., P.O.Box 481, Houston, TX 77001-0481*
† *Center for Wave Phenomena, Department of Geophysics, Colorado School of Mines, Golden, CO 80401-1887*

ABSTRACT

Processing of converted (PS) waves currently adopted by the exploration industry is essentially based on resorting the PS data into common conversion point gathers and using them for velocity analysis. Here we explore an alternative procedure. Our key idea is to generate the so-called *pseudo-shear* (ΨS) seismograms from the recorded PP and PS traces and run conventional velocity analysis on the reconstructed ΨS data. This results in an effective S-wave velocity model because our method creates data that possess kinematics of pure shear-wave primaries. We never deal with such complexities of converted waves as moveout asymmetry, reflection point dispersal, and polarity reversal, therefore, these generally troublesome features become irrelevant.

We describe the details of our methodology and examine its behavior both analytically and numerically. We apply the developed processing flow to a four-component ocean bottom cable line acquired in the Gulf of Mexico. Since the obtained stacking velocities of P- and ΨS-waves indicate the presence of effective anisotropy, we proceed with estimating a family of kinematically equivalent vertical transversely isotropic (VTI) velocity models of the subsurface.

1 INTRODUCTION

Due to a relatively high cost and usually poor quality of S-wave data excited on land and the absence of shear sources for marine surveys, converted (PS) waves are often used to infer shear-wave velocities in the subsurface. Processing of reflection PS data, however, is not straightforward. The main obstacle that precludes applying conventional velocity-analysis techniques to converted waves is the asymmetry of PS-wave reflection moveout on common-midpoint (CMP) gathers (e.g., Thomsen, 1999). As a consequence, neither a hyperbolic nor nonhyperbolic moveout equation routinely used for moveout correction of P-waves is generally expected to flatten PS data. Therefore, any technique designed for velocity estimation from reflected PS-waves should take into account the presence of some linear moveout at zero offset. This invariably complicates the moveout-estimation procedure for converted waves compared to that for pure modes and consequently decreases its robustness in the presence of noise. PS-wave processing is further compounded by polarity reversal and reflection (or conversion) point dispersal – phenomena that are almost nonexistent for conventional P-waves.

Recently, Grechka and Tsvankin (2002b) proposed a solution to the above outlined problems. Their $PP + PS = SS$ method uses traveltime picks of reflected PP and PS primaries from selected horizons to reconstruct traveltimes of the corresponding pure shear (SS) waves. Since the obtained S-wave moveouts are symmetric on CMP gathers, conventional velocity analysis can be applied to them. Implementation of the original, kinematic version of the method has two key elements: identifying PP and PS events reflected from the same interfaces (this is the only indirect velocity information required) and picking traveltimes from PP and PS prestack data.

In this paper, we make the $PP + PS = SS$ method more practical. We show that although an interpretive step of establishing the correspondence of PP and PS events cannot be avoided, the traveltime picking can. We develop a procedure that replaces the direct picking with a specially designed convolution of the original PP and PS traces. The result, which we call *pseudo-shear* (ΨS) data, has kinematics of pure S-wave primaries and, therefore, represents an appropriate input for conventional velocity analysis.

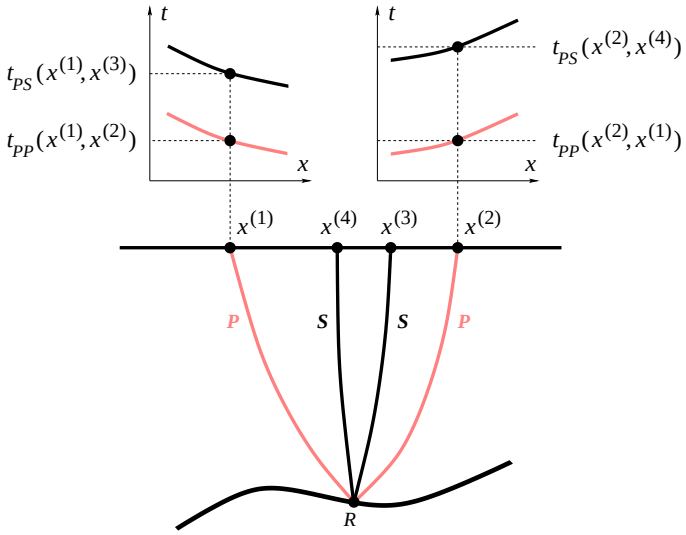

Figure 1. Ray diagram of the $PP + PS = SS$ method in 2-D (after Grechka and Tsvankin, 2002b).

We give the formulation of our procedure, explain why it works, and examine its performance on synthetic and field data. In particular, we demonstrate that our method is robust in the presence of random noise. Application of our technique to a 2-D multicomponent line acquired in the Gulf of Mexico indicates anisotropy and, therefore, requires building of at least a VTI (transversely isotropic with a vertical symmetry axis) velocity model. Although the narrow-azimuth nature of our data and the absence of substantial dip leads to a family of kinematically equivalent subsurface models (Grechka et al., 2002a, 2002b), we show that none of them is isotropic.

2 OVERVIEW OF THE $PP + PS = SS$ METHOD

A natural point of departure for our development is the kinematic conditions of $PP + PS = SS$ method (Grechka and Tsvankin, 2002b). Figure 1 shows PP and PS ray trajectories that the method finds from 2-D split-spread PP and PS reflection data. Three rays $x^{(1)}Rx^{(2)}$, $x^{(1)}Rx^{(3)}$, and $x^{(2)}Rx^{(4)}$ have exactly the same reflection point R if the pairs of PP and PS reflection slopes coincide at the P-wave source and receiver locations $x^{(1)}$ and $x^{(2)}$. Since by definition the slope $p(x^{(s)},x^{(r)})$ measured at source location $x^{(s)}$ on the common-receiver gather located at $x^{(r)}$ is

$$p(x^{(s)},x^{(r)}) = \frac{\partial t(x^{(s)},x^{(r)})}{\partial x^{(s)}} \qquad (1)$$

for any reflection mode, the requirement of equal PP and PS slopes yields

$$\frac{\partial t_{PP}(x^{(1)},x^{(2)})}{\partial x^{(1)}} = \frac{\partial t_{PS}(x^{(1)},x^{(3)})}{\partial x^{(1)}} \qquad (2)$$

and

$$\frac{\partial t_{PP}(x^{(2)},x^{(1)})}{\partial x^{(2)}} = \frac{\partial t_{PS}(x^{(2)},x^{(4)})}{\partial x^{(2)}}\,. \qquad (3)$$

Here t_{PP} and t_{PS} are the traveltimes of PP- and PS-waves, $x^{(j)}$ $(j = 1, 2, 3, 4)$ denote the source and receiver coordinates, and

$$t_{PP}(x^{(1)},x^{(2)}) = t_{PP}(x^{(2)},x^{(1)})$$

due to reciprocity. The geometry in Figure 1 produces the pure-S reflected ray $x^{(3)}Rx^{(4)}$. The traveltime t_{SS} along it is given by

$$t_{SS}(x^{(3)},x^{(4)}) = t_{PS}(x^{(1)},x^{(3)}) + t_{PS}(x^{(2)},x^{(4)}) - t_{PP}(x^{(1)},x^{(2)})\,. \qquad (4)$$

Clearly, one needs to pick prestack reflection traveltimes t_{PS} and t_{PP} along a selected horizon to calculate t_{SS} from equations (2)–(4). Although this is feasible in principle (Grechka et al., 2002a), prestack traveltime picking is known to be tedious, labor-intensive, and noise prone. Below, we describe a technique that not only makes traveltime picking unnecessary but also produces seismograms that resemble pure shear-wave reflection data for all horizons.

3 THEORETICAL ASPECTS OF GENERATING ΨS DATA

3.1 Statement of the result

It turns out that direct traveltime picking can be replaced by computing the integral

$$w_{\Psi S}(t,x^{(3)},x^{(4)}) = \iint \Big[\, w_{PS}(t,x^{(1)},x^{(3)}) * w_{PP}(-t,x^{(1)},x^{(2)}) * w_{PS}(t,x^{(2)},x^{(4)}) \Big]\, dx^{(1)}\, dx^{(2)}. \qquad (5)$$

Here w_{PP} and w_{PS} are the PP and PS seismic traces, t is time, and asterisks denote convolutions in time. The PP traces are taken in reverse time because the P-wave time gets subtracted in equation (4) to produce the pure-shear time. Integration is performed over P-wave source and receiver coordinates $x^{(1)}$ and $x^{(2)}$. The result of integration (5) is the ΨS trace for the source and receiver located at $x^{(3)}$ and $x^{(4)}$.

Evaluation of integral (5) using the stationary phase method (Appendix A) shows that if the traces w_{PP} and w_{PS} consist of PP and PS primaries corresponding to a selected reflector, the trace $w_{\Psi S}$ contains the pure S-wave primary from the same reflector. The fact that the proof in Appendix A is possible only for an isolated interface indicates the necessity for windowing the input w_{PP} and w_{PS} traces around events of interest. This in turn requires establishing the correspondence of PP and PS events prior to evaluating integral (5).

3.2 Amplitudes of ΨS-waves

Even though integral (5) produces ΨS data that ideally have traveltimes of pure S-waves, their amplitudes do not correspond to those of shear-wave primaries. This is immediately clear from equation (5). Indeed, the ΨS-wave amplitudes are inherited from those of the PP and PS events and, therefore, generating ΨS data is *not* a true-amplitude procedure. This is not surprising because, as follows from the reciprocity theorem, PP and PS data generally do not contain enough information for reconstructing the true S-wave amplitudes. The last statement can be illustrated by considering zero-offset PP and PS reflections from a single, sufficiently thick horizontal layer. The amplitude of reflected P-wave in this model is proportional to the P-wave impedance contrast at the interface, while the amplitude of converted wave is zero. Clearly, no information about the contrast of shear-wave impedance that governs amplitude of the pure S-wave can be extracted from the zero-offset PP and PS traces.

On the other hand, ΨS-wave amplitudes are obtained in a deterministic way from those of PP and PS reflections, therefore, they might be an attractive subject for amplitude-versus-offset (AVO) analysis. The benefits of using ΨS-waves instead of PS ones include the simplicity of their moveouts and usually higher signal-to-noise ratio than that of the original PP and PS data (see Figure 7 as an example). Below, however, we mostly ignore amplitude issues and concentrate primarily on velocity analysis of ΨS-waves. We will see that the described amplitude behavior does not cause any problem for obtaining accurate shear-wave stacking velocities.

3.3 Extension to 3-D

Similarly to the original $PP + PS = SS$ method of Grechka and Tsvankin (2002b), integral (5) can be extended to 3-D multiazimuth reflection data. Since the sources and receivers are now allowed to cover a certain area, their coordinates $\boldsymbol{x} \equiv [x_1, x_2]$ become two-dimensional vectors. The ΨS traces are formally given by the same equation (5)

$$w_{\Psi S}(t, \boldsymbol{x}^{(3)}, \boldsymbol{x}^{(4)}) = \iiiint \Big[w_{PS}(t, \boldsymbol{x}^{(1)}, \boldsymbol{x}^{(3)}) * w_{PP}(-t, \boldsymbol{x}^{(1)}, \boldsymbol{x}^{(2)}) * w_{PS}(t, \boldsymbol{x}^{(2)}, \boldsymbol{x}^{(4)}) \Big] d\boldsymbol{x}^{(1)} d\boldsymbol{x}^{(2)}, \quad (6)$$

where all $\boldsymbol{x}^{(j)}$ ($j = 1, 2, 3, 4$) are 2-D vectors and, therefore, integration becomes four-fold.

4 SYNTHETIC EXAMPLES

Here we present numerical tests that illustrate the above outlined theory in 2-D. We begin with examining the time function τ [equation (A5)] whose extrema determine kinematics of ΨS-waves, then compute integral (5) to study features of ΨS-data, and finally analyze the performance of our procedure in the presence of random noise.

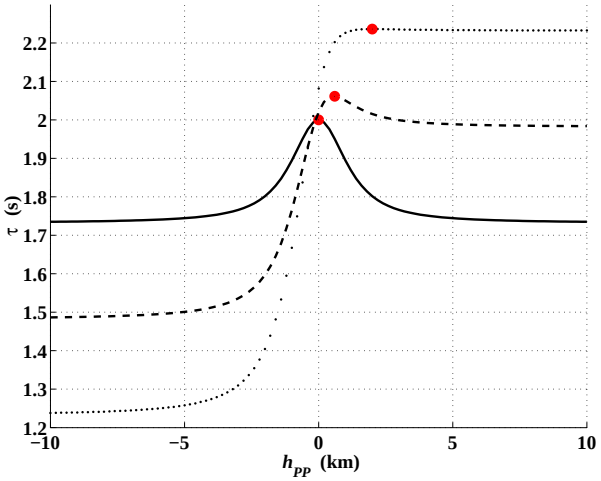

Figure 2. Time functions τ in a horizontal homogeneous isotropic layer that has the thickness $D = 1$ km and velocities $V_P = 2$ km/s and $V_S = 1$ km/s. Solid line corresponds to the ΨS-wave half-offset $h_{\Psi S} = 0$, dashed line to $h_{\Psi S} = 0.25$ km, and dotted line to $h_{\Psi S} = 0.5$ km. Large dots indicate stationary values of τ.

4.1 Time function τ

As follows from Appendix A, the ability of integral (5) to represent kinematics of S-waves depends upon the presence of roots $x^{(1)}$ and $x^{(2)}$ of equations (A6). Clearly, the PP and PS data are supposed to be physically recorded at the source and receiver locations $x^{(1)}$ and $x^{(2)}$ to contribute to the integral. Since the number of roots $x^{(1)}$ and $x^{(2)}$ and their very existence are unknown in advance, we present two examples that demonstrate what normally might be expected.

Defining the P-wave half-offset h_{PP} and the midpoint y_{PP} as

$$h_{PP} = \frac{x^{(2)} - x^{(1)}}{2} \quad \text{and} \quad y_{PP} = \frac{x^{(2)} + x^{(1)}}{2},$$

we plot the time functions $\tau(h_{PP}, y_{PP})$ in a plane homogeneous isotropic layer (Figure 2). The PP- and ΨS-wave midpoints, y_{PP} and

$$y_{\Psi S} = \frac{x^{(3)} + x^{(4)}}{2},$$

coincide because the layer is horizontal. As a consequence, the curves in Figure 2 were computed for the correct, i.e., stationary values $y_{PP} = y_{\Psi S}$. Figure 2 dis-

plays two clear maxima* of $\tau(h_{PP})$ for ΨS half-offsets $h_{\Psi S} = (x^{(3)} - x^{(4)})/2 = 0$ and $h_{\Psi S} = 0.25$ km (solid and dashed lines) and a poorly defined one for $h_{\Psi S} = 0.5$ km (dotted line). Those maxima, marked with large dots, produce stationary points that yield pure shear-wave reflection traveltimes. This statement can easily be verified by computing the S-wave moveout in our model (the parameters are given in the caption to Figure 2).

Note that the curves in Figure 2 flatten out at large P-wave half-offsets h_{PP} suggesting that the time function τ has extrema at $h_{PP} \to \pm\infty$. Although these extrema might seem irrelevant for the problem at hand because data are never acquired at infinite offsets, we will see that both the flatness of time function τ and finite frequency bandwidth of seismic data lead to noticeable contributions associated with those distant extrema even at relatively moderate h_{PP}.

The extrema at $h_{PP} \to \pm\infty$ relate to critical offsets of shear-waves (Figure 3). The P-wave incident and S-wave reflection angles, θ_P and θ_S, respectively, satisfy Snell's law

$$\frac{\sin\theta_P}{V_P} = \frac{\sin\theta_S}{V_S},$$

where V_P and V_S are the P- and S-wave velocities. Therefore, the maximum reflection angle of shear waves is $\theta_S^{crit} = \sin^{-1}(V_S/V_P)$. This yields the critical half-offset

$$h_{\Psi S}^{crit} = D \tan\left[\sin^{-1}\left(\frac{V_S}{V_P}\right)\right] \qquad (7)$$

in our simple model in Figure 3. Here D is the layer thickness. Since the P-wave half-offset corresponding to $h_{\Psi S}^{crit}$ is infinite, equation (7) establishes a physical limit of the maximum ΨS offset that can be obtained from PP and PS reflection data regardless their original offsets. Clearly, a low V_S/V_P velocity ratio results in a small spread of the ΨS data, thus, increasing the uncertainty of shear-wave velocity analysis. Our method explicitly shows the dependence of accuracy of the estimated shear-wave velocities on the V_S/V_P ratio, an issue that does not obviously follows from direct analysis of converted waves.

Figure 2 indicates that waves corresponding to the contributions of the flat areas of the time function $\tau(h_{PP})$ at $h_{PP} \to \pm\infty$ propagate with the P- rather than shear-wave velocity. For this reason, we will call them the ΨP-waves. Figure 2 also shows that the extrema of $\tau(h_{PP})$ corresponding to ΨS- and ΨP-waves approach each other in a continuous fashion and become indistinguishable as $h_{\Psi S} \to h_{\Psi S}^{crit}$ (dotted line). Since the ΨS and ΨP arrivals have different kinematics, mixing them together (under the improper name ΨS) will invariably lead to errors in the estimated S-wave velocities. The only remedy against that is to restrict integration in (5) to the half-offsets $h_{\Psi S} \le h_{\Psi S}^{crit}$.

*They are actually the saddle points. To show this, one needs to plot $\tau(h_{PP}, y_{PP})$ in the $[h_{PP}, y_{PP}]$ coordinates as done in Figure 4 below.

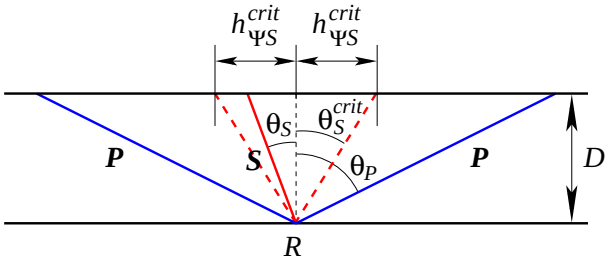

Figure 3. Critical ΨS-wave offset.

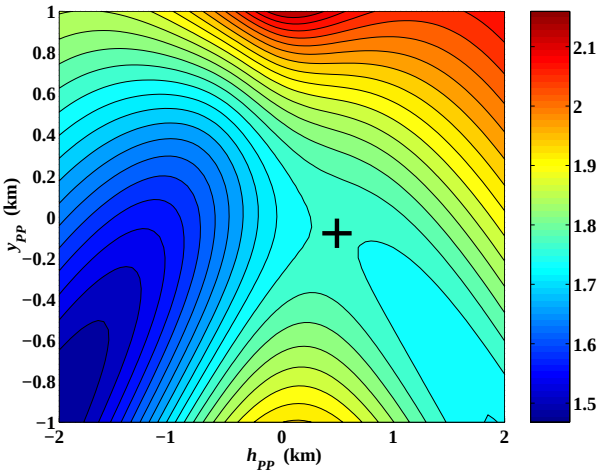

Figure 4. Time function $\tau(h_{PP}, y_{PP})$ (in s) for a dipping isotropic layer that has vertical thickness $D = 1$ km (under the coordinate origin $h_{PP} = y_{PP} = 0$), dip $\psi = 30°$ and the same velocities as those in Figure 2. The ΨS-wave midpoint and half-offset are $y_{\Psi S} = 0$ and $h_{\Psi S} = 0.2$ km, respectively.

Figure 4 gives an example of the time function $\tau(h_{PP}, y_{PP})$ for a dipping layer. The stationary (saddle) point corresponding to the ΨS arrival is located at $h_{PP} = 0.5$ km and $y_{PP} = -0.1$ km (cross in Figure 4); the common midpoints $y_{\Psi S}$ and y_{PP} are different due to the reflector dip. The flattening of the time function in the bottom corners of Figure 4 indicates approaching the extrema associated with ΨP-waves.

4.2 ΨS CMP gathers

Having learned that the integration limits in equation (5) need to be chosen properly to avoid mutual contamination of ΨS and ΨP data and also that convolutions have to be performed within time gates that enforce correlation of PP and PS events, we proceed with actual computation of ΨS seismograms.

Figures 5a and 5b show the input PP and PS traces, while Figure 5c demonstrates the result, a com-

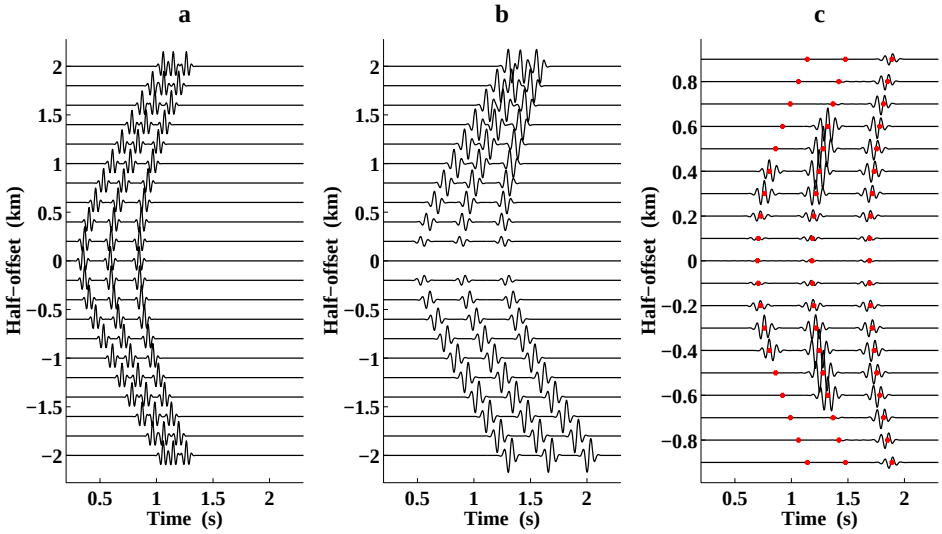

Figure 5. Input (a) PP, (b) PS, and (c) generated ΨS CMP gathers computed for midpoint at the origin. The model is homogeneous and isotropic with $V_P = 4$ km/s and $V_S = 2$ km/s. Three planar reflectors have the depths $D = 0.7$, 1.2, and 1.8 km beneath the origin; their dips are 0°, 10°, and 20°. Dots indicate correct S-wave reflection traveltimes.

puted ΨS CMP gather. The PP and PS data have the following features.

- PP and PS wavelets differ in both the shape and the frequency content; the ratio of dominant frequencies of PP- and PS-waves is 1.5.
- The polarity of reflected PS-waves flips at the zero offset.
- The converted-wave moveouts corresponding to dipping reflectors are asymmetric with respect to interchange of the source and receiver positions (Figure 5b). This phenomenon precludes applying conventional velocity analysis to PS data.

Figure 5c illustrates that the above features, which are usually troublesome for conventional converted-wave processing, do not prevent us from reconstructing meaningful ΨS data. The observation of primary importance in Figure 5c is that the reconstructed ΨS events follow correct (i.e., those computed by ray tracing) S-wave moveouts. The other features of ΨS are also worthwhile noting.

- As expected from the nature of convolution in equation (5), the ΨS wavelets are longer and have more lobes than do those of either PP or PS ones. Their dominant frequency lies between those of PP- and PS-waves.
- The ΨS CMP gather does not have polarity reversal. This follows from our formulation (5), which uses PS data twice so that the sign of PS polarity gets cancelled out.
- Weak amplitudes of ΨS-waves reconstructed at small offsets relate to the correspondingly weak PS signals. In particular, the PS amplitude is zero at $x^{(1)} = x^{(2)} = 0$. Since this is the stationary point for the output offset $X_{\Psi S} \equiv 2\,h_{\Psi S} = x^{(3)} - x^{(4)} = 0$, the zero-order term of the stationary phase method predicts a vanishing ΨS-wave amplitude. The weak ΨS arrivals observed at $h_{\Psi S} = 0$ in Figure 5c correspond to the contributions of higher-order terms in the stationary-phase expansion.
- The absence of ΨS-waves at large offsets is a result of limiting integration (5) to pre-critical offsets only. Specifically, our algorithm checks the value of $h_{\Psi S}$ and evaluates integral (5) only if $h_{\Psi S} \le h_{\Psi S}^{crit}$; otherwise it fills the output ΨS trace with zeros. Termination points for two shallow reflections in Figure 5c suggest that ΨS-waves can be reconstructed only for offset-to-depth ratios smaller than $X_{\Psi S}/D \approx 1$. This observation is in agreement with our theoretical result (7), which yields $X_{\Psi S}^{crit}/D = 2\,h_{\Psi S}^{crit}/D = 1.15$.

Following the discussion above, one might wonder what happens if we try to perform the same computation at half-offsets $h_{\Psi S} > h_{\Psi S}^{crit}$. Figure 6 addresses this question. We observe the events whose moveouts are approximately linear with the slopes $dt/dh_{\Psi S} \approx 2/V_P$ or $dt/dX_{\Psi S} \approx 1/V_P$. Clearly, their kinematics has nothing to do with that of reflected S-waves. This explains why we have chosen to call these arrivals the ΨP-waves. Only the changes in lengths of P-wave segments of converted-wave ray trajectories contribute to the moveouts in Figure 6 because the S-wave segments remain constant at any half-offset $h_{\Psi S} > h_{\Psi S}^{crit}$.

Since the ΨP-wave traveltimes are smaller than those associated with ΨS-waves (compare Figures 5c and 6), mixing the two events together and performing conventional velocity analysis will bias the estimated S-wave velocities towards higher values. As was already

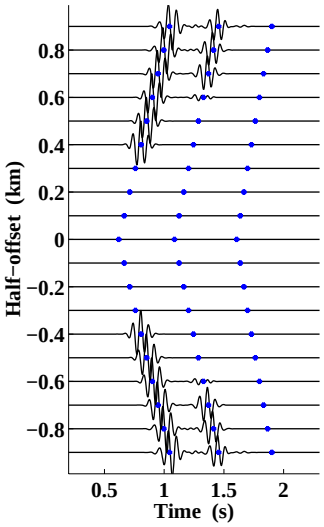

Figure 6. ΨP CMP gather generated from PP and PS data in Figure 5. Dots indicate the values of time function τ given by equation (A5) at its stationary points.

mentioned, we suggest to remove this bias by restricting integration in (5) to half-offsets $h_{\Psi S} \le h_{\Psi S}^{crit}$.

4.3 Influence of random noise

Since we intend to apply the discussed procedure to field data, it is important to examine its robustness with respect to noise. Figures 7a and 7b show PP and PS traces similar to those in Figures 5a and 5b but contaminated with Gaussian noise that has standard deviation equal to 1/2 of the maximum amplitude in the data. Even though the PP and PS reflections are hardly recognizable in Figures 7a and 7b, Figure 7c displays remarkably clean ΨS traces. Such a result is a direct consequence of applying convolutions, which efficiently attenuate random noise.

5 GULF OF MEXICO CASE STUDY

We tested our methodology on a multicomponent (hydrophone, vertical geophone, and inline horizontal geophone) 2-D line acquired in the Gulf of Mexico. First, the PP-to-PS event correspondence was established. This gave us the relationship between PP and PS zero-offset times, t_{PP0} and t_{PS0}, which were used to compute the shear-wave traveltimes t_{SS0} and the ratios g_0 as

$$g_0(t_{PP0}) \equiv \frac{t_{PP0}}{2\,t_{PS0} - t_{PP0}} = \frac{t_{PP0}}{t_{SS0}}\,. \tag{8}$$

The result of our computations is shown in Figure 8. Due to mild lateral heterogeneity of the subsurface, both functions $t_{SS0}(t_{PP0}, Y)$ and $g_0(t_{PP0}, Y)$ have a relatively weak dependence on the CMP coordinate Y.

An important observation that can be made from Figure 8b is that the ratio g_0 is quite small (about 0.15) at shallow depths. If we ignore the possible presence of anisotropy, reflector dip, and lateral heterogeneity, and use the value of $g_0 = V_S/V_P = 0.15$ to estimate the critical ΨS offset-to-depth ratio from equation (7), we find $X_{\Psi S}^{crit}/D = 2\,h_{\Psi S}^{crit}/D \approx 0.3$. Clearly, shear-wave stacking velocities cannot be picked accurately from such short-spread moveouts. The ratio g_0, however, rapidly increases as we go deeper, reaching the value of $g_0 = 0.35$ at t_{PP0} of around 5.5 s. This yields the ratio $X_{\Psi S}^{crit}/D \approx 0.75$ which makes the results of ΨS-wave velocity analysis substantially more accurate despite the influence of growing $V_S(t_{SS0})$ that flattens ΨS moveouts and, therefore, tends to reduce the accuracy of velocity picking.

Figure 9, which displays the generated ΨS data, corroborates the above discussion. Indeed, we observe a rapid increase of the maximum ΨS-wave offset as the time t_{SS0} grows. Velocity analysis performed on ΨS CMP gathers such as those in Figure 9 produces poorly resolved semblance maxima at shear times t_{SS0} smaller than about 5-6 s (not shown). This, however, is a consequence of low V_S/V_P ratio in the shallow layers rather than a deficiency of the applied procedure. The semblance maxima of ΨS-waves become better focused as t_{SS0} exceeds 6-7 s, which corresponds to P-wave times t_{PP0} between 2 and 3 s. The results of velocity analysis on PP and ΨS CMP gathers (Figure 10) are used below to estimate the interval velocities.

5.1 Evidence for effective anisotropy

Prior to estimating the interval-velocity model, one usually needs to understand which its features are constrained by the available data. Here, we show that the event correlation (Figure 8) and the picked normal-moveout (NMO) velocities (Figure 10) unambiguously indicate non-negligible anisotropy. To draw such a conclusion, we essentially rely on the fact that the subsurface structure, being characterized by weak lateral heterogeneity and mild dip (see Figure 13 below), is approximately one-dimensional.

Following Grechka et al. (2002a), let us examine two velocity ratios: g_0, which is equal to the ratio of the vertical velocities V_{S0} and V_{P0} for a horizontally layered media,

$$g_0 \equiv \frac{t_{PP0}}{t_{SS0}} = \frac{V_{S0}}{V_{P0}}\,, \tag{9}$$

and

$$g_{\rm nmo} \equiv \frac{V_{S,\rm nmo}}{V_{P,\rm nmo}}\,. \tag{10}$$

The ratio g_0 derived from the PP and PS event correlation is shown in Figure 8b, while the ratio of ΨS- and P-wave NMO velocities is given in Figure 11. Comparing the two, we observe that $g_{\rm nmo}$ is consistently greater

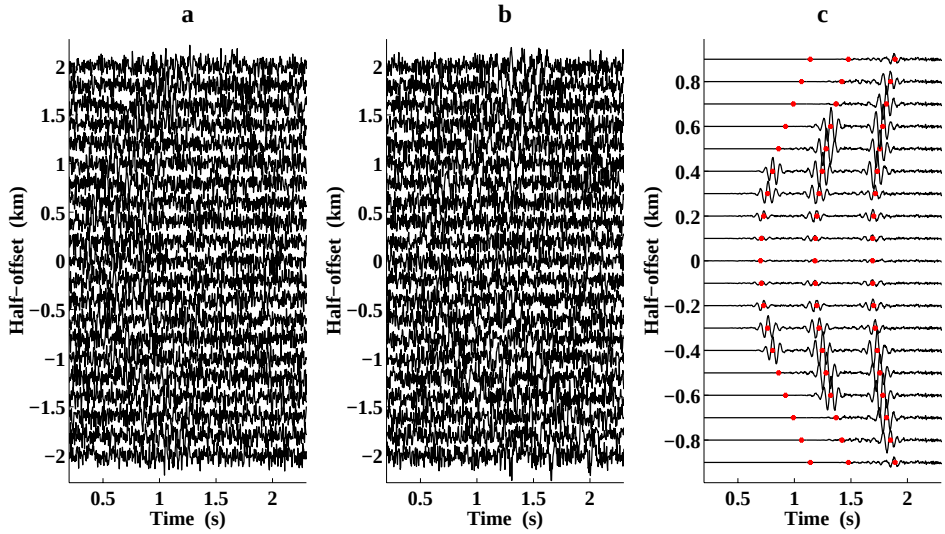

Figure 7. Same as Figure 5 but for PP and PS data contaminated with Gaussian noise that has signal-to-noise ratio equal to 2. Dots indicate correct S-wave reflection traveltimes.

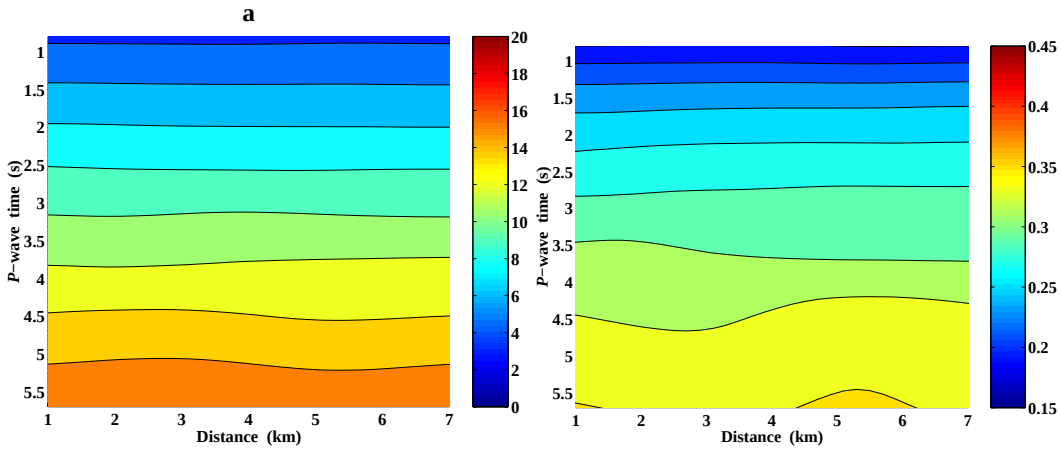

Figure 8. Event correlation displayed (a) as function $t_{SS0}(t_{PP0}, Y)$ and (b) as ratio $g_0(t_{PP0}, Y)$. Here t_{SS0} and t_{PP0} are the S- and P-wave two-way zero-offset times (in s), respectively, and Y is the distance (in km) along the line or the CMP coordinate. The color bars refer to the values of t_{SS0} (a) and g_0 (b).

than g_0. For the P-wave times $t_{PP0} > 2.5$ s, where we expect the ΨS-wave NMO velocities to be sufficiently accurate, $g_0 \approx 0.3$ whereas $g_{\rm nmo} \approx 0.4$.

In isotropic layered media, $g_{\rm nmo}$ can be greater than g_0 only because of larger vertical variability of S-wave velocities compared to that of the P-wave ones. According to Grechka et al. (2002a), relative vertical changes of V_{S0} are supposed to be factors of magnitude greater than those of V_{P0} to explain the observed values of g_0 and $g_{\rm nmo}$. Since such a high vertical heterogeneity of shear-waves is not supported by the data, only the presence of anisotropy can give plausible explanation for the difference between the two velocity ratios. Therefore, the reconstructed subsurface model has to be anisotropic. Next, we need to choose the type of anisotropy. This choice is essentially governed by our ability to estimate relevant anisotropic parameters from given 2-D narrow-azimuth data and a relatively simple (close to 1-D) subsurface structure. Taking into account that the data were acquired in a sedimentary basin, transversely isotropic model with a vertical symmetry axis (VTI) is a proper choice. Also, we assume that we are dealing with SV-waves because converted waves recorded on inline horizontal component were used to generate the ΨS data.

The ratios g_0 and $g_{\rm nmo}$ defined by equations (9) and (10) can be directly linked to anisotropic coefficients δ (Thomsen, 1986) and σ (Tsvankin and Thom-

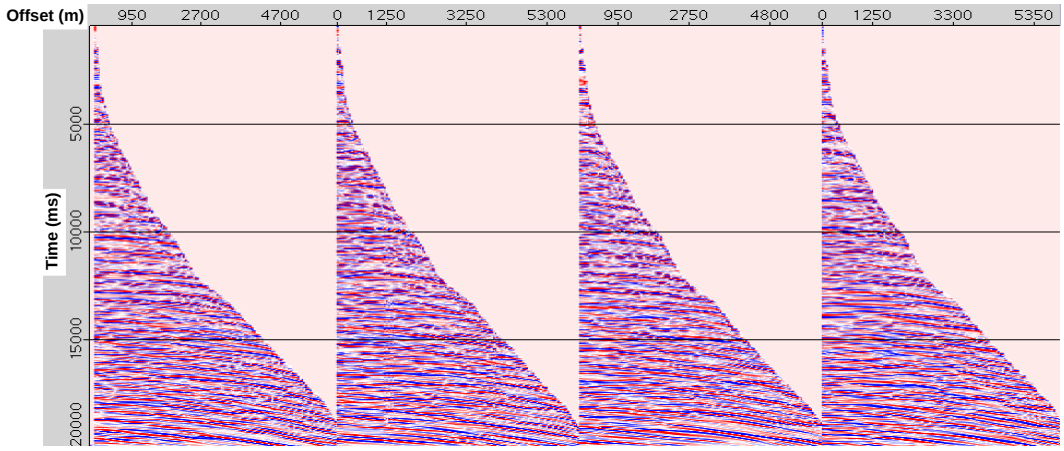

Figure 9. Typical ΨS CMP gathers.

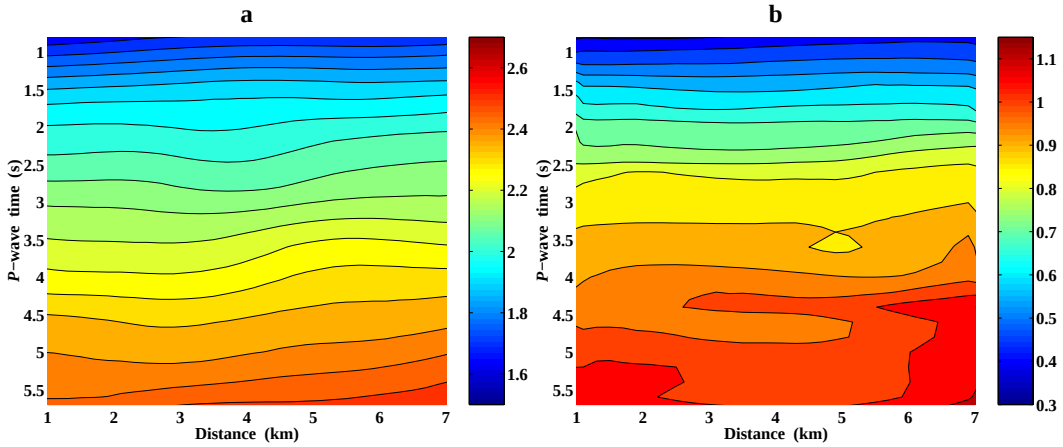

Figure 10. Picked (a) PP- and (b) ΨS-wave NMO velocities (in km/s).

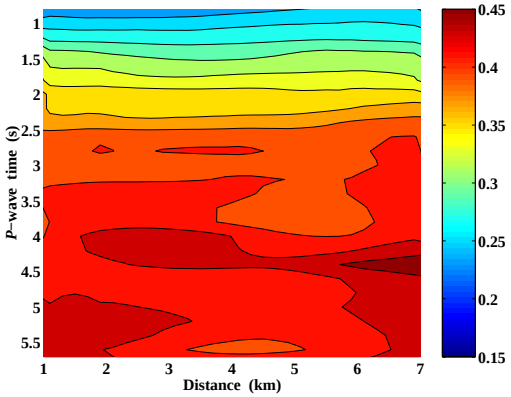

Figure 11. Ratio $g_{\rm nmo}$ of the picked ΨS- and P-wave NMO velocities. For comparison, the color scale in this figure is the same as that in Figure 8b.

sen, 1994) in a single plane VTI layer. Since $V_{P,\rm nmo} = V_{P0}\sqrt{1+2\,\delta}$ and $V_{S,\rm nmo} = V_{S0}\sqrt{1+2\,\sigma}$, the combination

$$\frac{1}{2}\left(\frac{g_{\rm nmo}^2}{g_0^2}-1\right) = \frac{\sigma-\delta}{1+2\,\delta} \equiv \chi \qquad (11)$$

depends solely on δ and σ and, therefore, quantifies the effective anisotropy that can be unambiguously estimated from PP and PS event correlation and the NMO velocities of P- and SV-waves in a plane homogeneous VTI layer. Because $g_0 \neq g_{\rm nmo}$ for our data, $\chi \neq 0$ (Figure 12), again supporting our conclusion that the subsurface is effectively anisotropic.

5.2 Estimation of interval parameters

The feasibility of estimating anisotropy from reflection seismic data is governed by the amount of angular information that can be used in the inversion. Both acquisition design and the presence or absence of dipping

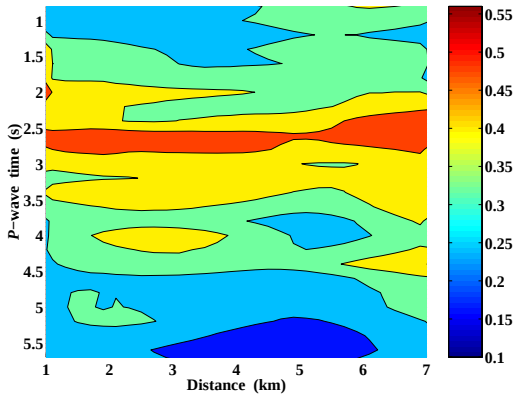

Figure 12. Effective χ defined by equation (11).

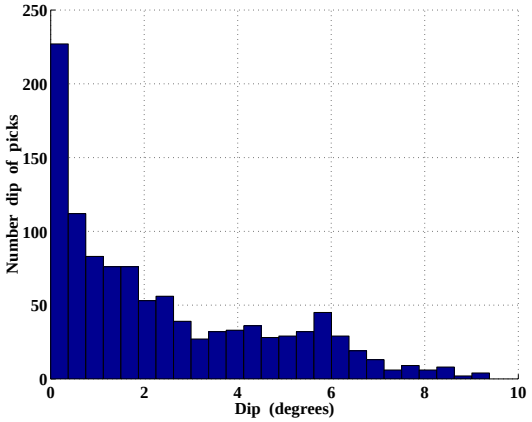

Figure 13. Distribution of dips picked from the P-wave zero-offset time section.

structures influence angular coverage of the subsurface. While 3-D, wide-azimuth, long-spread data generally constrain anisotropic parameters better than do 2-D, narrow-azimuth, conventional-offset data, all pertinent quantities still cannot be estimated uniquely in horizontally layered VTI media unless check shots or well logs are available (e.g., Grechka and Tsvankin, 2002a; Grechka et al., 2002b). Therefore, it is important to examine whether or not our data contain enough dip information for the inversion.

Figure 13 addresses this issue. It shows a histogram of more than thousand dips ψ automatically picked from the stacked PP data. Even though we estimated the dips using the equation

$$\psi = \tan^{-1}\left[\left|\frac{dt_{PP0}}{dY}\right| \frac{V_{P,\mathrm{nmo}}}{2}\right]$$

which ignores anisotropy and heterogeneity, the message communicated by Figure 13 is clear. The subsurface can be treated as horizontally layered for the purpose of anisotropic inversion because the mean absolute dip is about 2.5° and 50% of our picks fall below 1.7°.

As Grechka and Tsvankin (2002a) show, the true depths in horizontally layered VTI media cannot be estimated from reflected PP- and PS-waves even when long-spread data are available. Therefore, we essentially have the following two choices. We could set either anisotropic coefficient δ or σ to any chosen constant value or any predetermined function and proceed with anisotropic stacking velocity tomography as was done by Grechka et al. (2002a). The arbitrariness in δ or σ will produce a family of kinematically equivalent VTI depth models. Alternatively, we can perform parameter estimation in time domain that targets the interval NMO velocities $V_{P,\mathrm{nmo}}$, $V_{S,\mathrm{nmo}}$, and the quantity χ treated as functions of the P-wave vertical time t_{PP0}. This yields a unique VTI time model, with the above mentioned ambiguity hidden in the time-to-depth conversion. We select this option here.

Figures 14a and 14b show the interval $V_{P,\mathrm{nmo}}$ and $V_{S,\mathrm{nmo}}$ that were obtained by performing conventional Dix (1955) differentiation of the NMO velocities displayed Figure 10. The interval anisotropy χ in Figure 14c was computed from the interval ratios g_{nmo} and the event correspondence (Figure 8). Even though the higher χ values for $t_{PP0} < 2.5$ s seem to relate to inaccuracies in shear-wave velocity picking, we again observe non-negligible anisotropy.

Note that the inversion produces similarly dipping features in the middle of the $V_{P,\mathrm{nmo}}$, $V_{S,\mathrm{nmo}}$, and χ sections. Such kind of general similarity is expected because the three fields correspond to the same area of the subsurface. The sections of $V_{P,\mathrm{nmo}}$, $V_{S,\mathrm{nmo}}$, and χ, however, differ in many details. This also could have been predicted because they represent different physical properties obtained from different components of seismic data which went through different processing sequences. Still, in some sense, the three sections in Figure 14 complement each other, thus, providing information that cannot be extracted from P-wave data alone.

Even though Figure 14 displays our final output, it hides significant depth ambiguity of the estimated anisotropic models. Since the pairs $\{t_{PP0}, V_{P,\mathrm{nmo}}\}$ and $\{t_{SS0}, V_{S,\mathrm{nmo}}\}$ have been obtained, we would still need to fix either anisotropic coefficient δ or σ in order to perform time-to-depth conversion. Neither of these coefficient, however, can be estimated from the data. Instead, we can constrain only their combination $\chi = (\sigma-\delta)/(1+2\,\delta)$ which does not allow us to resolve δ and σ individually, as a consequence, the true depth remains unknown. One might notice an analogy between this conclusion and nonhyperbolic velocity analysis of P-waves, where the estimated $V_{P,\mathrm{nmo}}$ and the Alkhalifah-Tsvankin (1995) anellipticity coefficient η also tell us nothing about the depth.

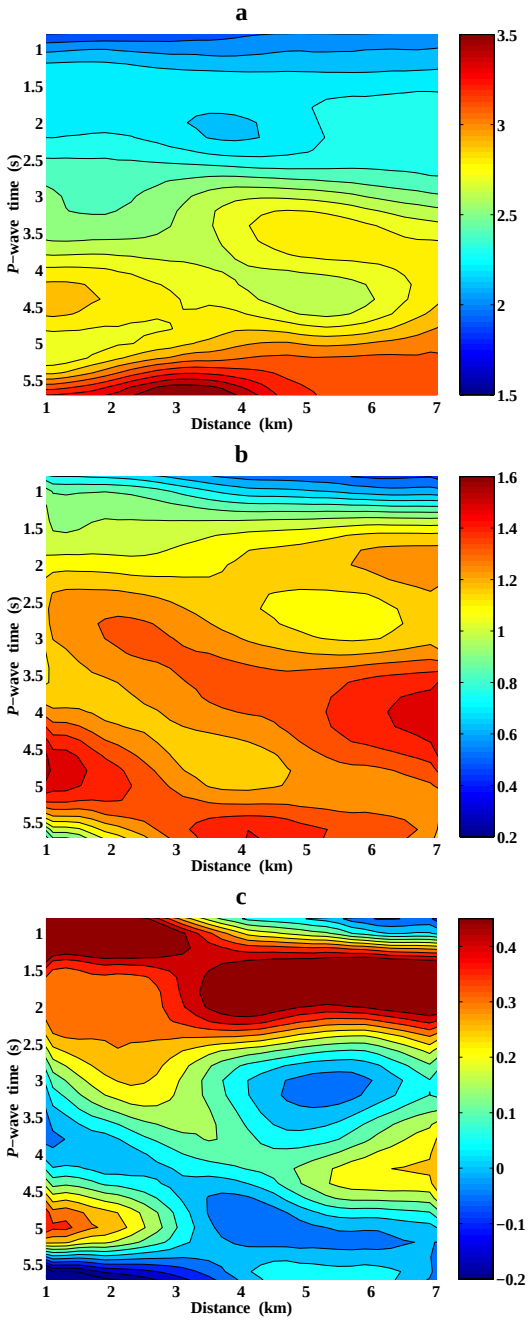

Figure 14. Interval (a) P- and (b) ΨS-wave NMO velocities (in km/s), and (c) χ.

6 DISCUSSION AND CONCLUSIONS

We described the processing flow designed for velocity analysis of converted waves. Under the assumptions that (i) both PP and PS reflection data are available and (ii) the PP and PS event correspondence is established, we developed an automatic procedure for generating the ΨS data that ideally have kinematics of pure shear-wave primaries. As a result, conventional velocity analysis performed on ΨS CMP gathers yields S-wave NMO velocities. These velocities, along with those of the P-waves and the corresponding reflection dips, can be used for building elastic (usually anisotropic) interval-velocity models. Analyzing this final step, however, is outside the scope of our paper.

To construct the ΨS data, one has to integrate specially designed convolutions of PP and PS traces [equations (5) and (6) in 2-D and 3-D, respectively]. We found, however, that successful implementation of the technique requires selecting time gates that enforce the correspondence of PP and PS events and restricting the integration limits. While the time gates are needed to avoid generating artificial multiples and unphysical events (Grechka and Tsvankin, 2002b), choosing the limits of integration around proper stationary points ensures that the output traces are not contaminated with ΨP-waves and other unwanted arrivals. One conclusion we drew along the way was that the spread of ΨS data is always limited by the critical offset. Although this result directly follows from Snell's law, it has the following important practical implication. When the S- to P-wave velocity ratio is small, the correspondingly small ratio of maximum ΨS offset to reflector depth will invariably compromise the quality of shear-wave velocity analysis.

We tested our methodology on both synthetic and field data. While synthetic examples helped us to establish some data requirements and characteristics (e.g., PP and PS wavelets do not have to be the same, and random noise is not a problem), the presented case study also demonstrated that our processing flow can produce useful results.

A relevant issue we have not discussed in detail relates to the errors in establishing event correspondence. Substantial errors in relating the events to the same reflector lead to convolving wrong PP and PS arrivals and, therefore, produce S-wave NMO velocities that can be significantly incorrect. Sometimes those errors are relatively easy to recognize. We have examined the influence of small deviations from correct event correspondence on the output shear-wave zero-offset times and NMO velocities. We found that the ratio of errors in t_{SS0} and $V_{S,\mathrm{nmo}}$ is always positive. Therefore, when the velocity $V_{S,\mathrm{nmo}}(t_{SS0})$ grows (which is often the case), it is not going to be severely distorted because erroneous values of $V_{S,\mathrm{nmo}}$ and t_{SS0} will fall relatively close to the correct trend $V_{S,\mathrm{nmo}}(t_{SS0})$.

We have left a few issues almost completely undeveloped. First, almost horizontally propagating ΨP-waves generated by our procedure might be used to get more accurate estimates of anisotropic coefficient η than those obtained from P-wave nonhyperbolic moveout. A similar idea, although for PS- rather than ΨP-waves, was proposed by Grechka and Tsvankin (2002a). They noticed that longer and closer to horizontal P-ray segments in PS data compared to those in PP ones more

tightly constrain η. A second potential research area lies in making use of ΨS-wave AVO behavior to extract the PS AVO signature. As we already stated, an apparent advantage of dealing with ΨS rather than with PS data includes their simpler moveouts and usually higher signal-to-noise ratio. Finally, generating ΨS-waves and estimating shear-wave velocities provides solid ground for performing migration of ΨS data. This has not been done so far, therefore, it remains to be seen what can be gained from the ΨS images.

ACKNOWLEDGEMENTS

The idea of implementing the $PP + PS = SS$ method as a series of convolutions was first proposed by Joe Dellinger (BP) and Helmut Jakubowicz (Veritas) at the Center for Wave Phenomena (CWP) meeting in 2001, where kinematics of the method was presented. We thank Shell International E & P Inc. for permission to publish the paper. We are grateful to members of the PSDM team at Bellaire Technology Center and to members of the A(nisotropy)-Team at the CWP, Colorado School of Mines, for helpful discussions. We thank Adam Chow and Jon Sheiman (both Shell) for preprocessing the field data discussed in the paper. We appreciate the excellent feedback of Ken Larner, Ilya Tsvankin (both CWP), Joe Dellinger (BP), and Andrey Bakulin (Shell), who reviewed the manuscript. Support for Pawan Dewangan was partially provided by the Chemical Sciences, Geosciences and Biosciences Division, Office of Basic Energy Sciences, U.S. Department of Energy.

REFERENCES

Alkhalifah, T., and Tsvankin, I., 1995, Velocity analysis for transversely isotropic media: Geophysics, **60**, 1550–1566.

Dix, C.H., 1955, Seismic velocities from surface measurements: Geophysics, **20**, 68–86.

Grechka, V., and Tsvankin, I., 2002a, The joint nonhyperbolic moveout inversion of PP and PS data in VTI media: Geophysics, **67**, 1929–1932.

Grechka, V., and Tsvankin, I., 2002b, $PP+PS = SS$: Geophysics, **67**, 1961–1971.

Grechka, V., Tsvankin, I., Bakulin, A., and Hansen, J.O., 2002a, Joint inversion of PP and PS reflection data for VTI media: A North Sea case study: Geophysics, **67**, 1382–1395.

Grechka, V., Pech, A., and Tsvankin, I., 2002b, Multicomponent stacking-velocity tomography for transversely isotropic media: Geophysics, **67**, 1564–1574.

Thomsen, L., 1986, Weak elastic anisotropy: Geophysics, **51**, 1954–1966.

Thomsen, L., 1999, Converted-wave reflection seismology over inhomogeneous, anisotropic media: Geophysics, **64**, 678–690.

Tsvankin, I., and Thomsen, L., 1994, Nonhyperbolic reflection moveout in anisotropic media: Geophysics, **59**, 1290–1304.

APPENDIX A: KINEMATICS OF ΨS-WAVES

Here we prove that integral (5) produces waves that have kinematics of pure-S primaries when the input PP and PS traces contain primaries only. Applying the Fourier transform to equation (5) yields

$$W_{\Psi S}(\omega, x^{(3)}, x^{(4)}) = \iint \Big[\, W_{PS}(\omega, x^{(1)}, x^{(3)}) \times W^{\star}_{PP}(\omega, x^{(1)}, x^{(2)})\, W_{PS}(\omega, x^{(2)}, x^{(4)}) \Big] dx^{(1)} dx^{(2)}, \quad \text{(A1)}$$

where ω is radial frequency, W_{PP}, W_{PS}, and $W_{\Psi S}$ are the spectra of PP, PS, and ΨS traces, respectively, and star denotes complex conjugate.

If we assume that the input PP and PS traces consist of primaries reflected from a given interface, their spectra have the form

$$W^{\star}_{PP}(\omega, x^{(1)},\, x^{(2)}) = F^{\star}_{PP}(\omega)\, A^{\star}_{PP}(x^{(1)},\, x^{(2)}) \times e^{-i\,\omega\, t_{PP}(x^{(1)},\, x^{(2)})} \quad \text{(A2)}$$

and

$$W_{PS}(\omega, x^{(s)},\, x^{(r)}) = F_{PS}(\omega)\, A_{PS}(x^{(s)},\, x^{(r)}) \times e^{i\,\omega\, t_{PS}(x^{(s)},\, x^{(r)})}. \quad \text{(A3)}$$

Here A_{PP} and A_{PS} represent the amplitudes of reflected PP- and PS-waves, F_{PP} and F_{PS} denote the spectra of their wavelets, and indexes r and s take the pairs of values $\{s = 1,\ r = 3\}$ and $\{s = 2,\ r = 4\}$. Substituting equations (A2) and (A3) into integral (A1), we obtain

$$W_{\Psi S}(\omega, x^{(3)}, x^{(4)}) = F^2_{PS}(\omega)\, F^{\star}_{PP}(\omega) \times \iint \Big[\, A_{PS}(x^{(1)},\, x^{(3)})\, A^{\star}_{PP}(x^{(1)},\, x^{(2)})\, A_{PS}(x^{(2)},\, x^{(4)}) \times\ e^{i\,\omega\,\tau} \Big]\, dx^{(1)}\, dx^{(2)}. \quad \text{(A4)}$$

The time τ in this equation is given by

$$\begin{aligned} \tau \ &\equiv \tau(x^{(1)}, x^{(2)}, x^{(3)}, x^{(4)}) \\ &= t_{PS}(x^{(1)}, x^{(3)}) + t_{PS}(x^{(2)}, x^{(4)}) \\ &\quad - t_{PP}(x^{(1)}, x^{(2)}). \end{aligned} \quad \text{(A5)}$$

Since our goal is to show that the ΨS event has kinematics of pure-S primary, we need to evaluate integral (A4) in the limit of $\omega \to \infty$. This can be done with the stationary phase method. According to this method, the main contributions to the integral occur around points $\left\{x^{(1)}, x^{(2)}\right\}$ that satisfy the conditions of stationarity

$$\frac{\partial \tau}{\partial x^{(1)}} = \frac{\partial \tau}{\partial x^{(2)}} = 0. \quad \text{(A6)}$$

Let us note that equations (A6) coincide with expressions (2) and (3) representing the requirements of matching reflection slopes of reflected PP- and PS-waves (Figure 1). If equations (A6) have a solution

$$\left\{x^{(1)}, x^{(2)}\right\} \equiv \left\{x^{(1)}(x^{(3)}, x^{(4)}),\, x^{(2)}(x^{(3)}, x^{(4)})\right\}\,, \quad \text{(A7)}$$

the time function τ defined by equation (A5) becomes equal to the traveltime t_{SS} given by formula (4). Therefore, kinematics of a pure-S primary is, indeed, represented by integral (A4) in the high-frequency limit.